Breaking the Stoichiometric Limit in Oxygen Carrying Capacity of Fe-based Oxygen Carriers for Chemical Looping Combustion using the Mg-Fe-O Solid Solution System

Qianwenhao Fan,[1,2] Chuande Huang,[3] Shibo Xi,[4] Yong Yan,[1] Jijiang Huang,[5] Saqline Syed,[1,2,5] Longgang Tao,[1] Yihu Dai,[6] Armando Borgna,[4] Xiaodong Wang,[3]* and Wen Liu[1,2,5]**

[1] School of Chemical and Biomedical Engineering, Nanyang Technological University, 62 Nanyang Drive, Singapore 637459, Singapore

[2] Cambridge Centre for Advanced Research and Education in Singapore, 1 Create Way, Singapore 138602, Singapore

[3] Dalian Institute of Chemical Physics, Chinese Academy of Sciences, 457 Zhongshan Road, Dalian 116023, People's Republic of China

[4] Institute of Chemical and Engineering Sciences, Agency for Science, Technology and Research, 1 Pesek Road, Singapore 627833, Singapore

[5] Nanyang Environmental and Water Research Institute, Nanyang Technological University, 1 Cleantech Loop, Singapore 637141, Singapore

[6] Institute of Advanced Synthesis, School of Chemistry and Molecular Engineering, Nanjing Tech University, Nanjing 211816, China

Corresponding Author

* Corresponding authors: huangchuande@dicp.ac.cn (Chuande Huang), xdwang@dicp.ac.cn (Xiaodong Wang), wenliu@ntu.edu.sg (Wen Liu)

ABSTRACT

The performance of oxygen carriers contributes significantly to the efficiency of chemical looping combustion (CLC), an emerging carbon capture technology. Despite the low-cost, Fe_2O_3-based oxygen carriers suffer from sintering-induced deactivation and low oxygen carrying capacity (OCC) during CLC operations. Here, we report the development of a sintering-resistant MgO-doped Fe_2O_3 oxygen carrier with an optimal composition of $5MgO•MgFe_2O_4$, which exhibits superior cyclic stability and an OCC of 0.45 mol O/mol Fe (2.25 mmol O/g_{solid}), exceeding the widely accepted OCC limit of 0.167 mol O/mol Fe (2.08 mmol O/g_{solid}) of unmodified commercial Fe_2O_3. This result distinguishes from all past studies, in which efforts to enhance the cyclic stability of Fe-based oxygen carriers would always result in dilution of the OCC. The capacity enhancement by MgO is attributed to the unique mixtures of $Mg_xFe_{1-x}O$ (halite) and $Mg_{1-y}Fe_{2+y}O_4$ (spinel) solid solutions, which effectively reduce the exergonicity for the reduction from Fe^{3+} to Fe^{2+}, whilst preventing any irreversible structural transformations during the redox process. This hypothesis-driven oxygen carrier design approach provides a new avenue for tailoring the lattice oxygen activities of oxygen carriers for chemical looping applications.

KEYWORDS

chemical looping combustion, oxygen carriers, phase diagram, solid solution, mixed spinel

INTRODUCTION

Climate change caused by the emission of greenhouse gases, in particular CO_2, is one of the greatest challenges to mankind in the present century. Carbon capture and storage is a promising solution to decarbonize the modern economy. However, the state-of-the-art carbon capture approaches, e.g., post-combustion,[1, 2] pre-combustion,[3, 4] and oxy-combustion,[5, 6] are often associated with significant energy efficiency penalties. Chemical looping combustion (CLC)[7] is an emerging carbon capture technology that combusts hydrocarbon fuels in the absence of nitrogen. This is achieved using a solid carrier material (oxygen carrier), which transports oxygen from air to fuels in the form of lattice oxygen. As depicted in Figure 1a, a CLC process generally consists of a reduction half-cycle, where the oxygen carrier provides lattice oxygen to combust fuels, and a subsequent oxidation half-cycle of carrier regeneration using air. In doing so, the combustion (taking place in the fuel reactor) produces only CO_2 and H_2O. After steam condensation, the CO_2 is considered captured and can be readily exported for sequestration or utilization. Thus, the need for gas separation and the associated energy penalty is inherently avoided. Compared to competing carbon capture approaches, CLC is also exergetically efficient, because the redox reactions and heat exchanges take place at close-to-equilibrium conditions.[8]

Over the past two decades, CLC has been demonstrated at increasingly large scales,[9] whilst the performance of oxygen carriers is continuously improved. Qualifying oxygen carrier materials must have suitable thermodynamic properties to facilitate (i) complete fuel combustion in the presence of high CO_2 concentration, (ii) regeneration of lattice oxygen in air. Besides, they should also possess sufficiently high oxygen carrying capacity (OCC), long-term stability over redox cycles, low toxicity, and can be produced at large scales at reasonably low costs.[10] These criteria narrow the candidate oxygen carrying materials to the oxides of the 3d transition metals, most notably Mn_2O_3,[11] Fe_2O_3,[12] Co_3O_4,[13] NiO,[14] CuO[15] and their synthetic or natural derivatives.

The low price and environmentally friendly nature of Fe_2O_3 make it one of the most studied oxygen carrier materials amongst the 3d transition metal oxides.[16] However, the OCC of the Fe_2O_3/Fe_3O_4 redox couple is low compared to that of NiO/Ni, CuO/Cu, Mn_2O_3/Mn_3O_4, and Co_3O_4/CoO, because the reduction of Fe_3O_4 to FeO and ultimately Fe is thermodynamically prohibited under the operation conditions commonly observed in typical fuel reactors, which often take the form of bubbling fluidized beds.[17] Although more advanced reactor designs, such as cascade counter current moving beds may be able to achieve higher utilization of the lattice oxygen in Fe-based oxygen carriers (up to 0.75 mol O/mol Fe),[18] the reaction rates in all fuel reactor designs would ubiquitously limited by the low reducibility of Fe_3O_4. Such limitation arises from the fact that the inverse spinel structure of Fe_3O_4 is thermodynamically stable and cannot be easily reduced further. Furthermore, all 3d transition metal oxides ubiquitously suffer from sintering over CLC cycles,[19, 20] which take place at temperatures exceeding the Hüttig and Tamman temperatures of the transition metal oxides, especially in their reduced form. In order to improve the cyclic stability and mechanical strength of the oxygen carriers, the redox active components, i.e., the transition metal oxides, are often supported on refractory ceramics, such as SiO_2,[21] TiO_2,[22] MgO, Al_2O_3,[23, 24] $MgAl_2O_4$, and ZrO_2.[25, 26] As these refractory materials generally exhibit significantly low redox activities, the improvements in cyclic stability often come at the expense of reduced oxygen carrying capacity. Alternatively, the redox activities of the transition metal oxides can be modified by preparing ternary mixed oxide phases such as perovskites.[27, 28] Again, the oxygen carrying capacity of perovskite-type oxides are diluted by the A-site cations, which are typically redox-inert. Therefore, it remains challenging to improve the oxygen carriers' performance, in terms of both cycling stability and redox activity, using easily accessible doping materials and green synthesis routes.

In this study, we report a novel strategy to enhance the performance of Fe_2O_3-based oxygen carriers by exploiting solid solution effects between oxides of Fe and MgO. We studied the

Mg-Fe-O system and have identified $5MgO•MgFe_2O_4$ (3M1F) as an optimal oxygen carrier formulation for CLC. The 3M1F oxygen carrier was experimentally validated by 100 CLC cycles at 850 °C using a 9:1 mixture of CO_2 and CO as the fuel. This material, bearing only 40 wt% of Fe_2O_3, exhibits an OCC of 2.26 mmol O/g when reduced in a differential packed bed; this is notably higher than the stoichiometric maximum OCC of pure Fe_2O_3 of 2.08 mmol O/g when it is reduced under identical reaction conditions. Detailed investigation of the structures of the solid solution-based oxygen carrier reveals that such capacity enhancement originates from the interaction between $Mg_xFe_{1-x}O$ (halite) and $Mg_{1-y}Fe_{2+y}O_4$ (spinel) solid solutions, which significantly improves the reducibility of Fe^{3+} in the oxygen carrier and promotes the supply of lattice oxygen.

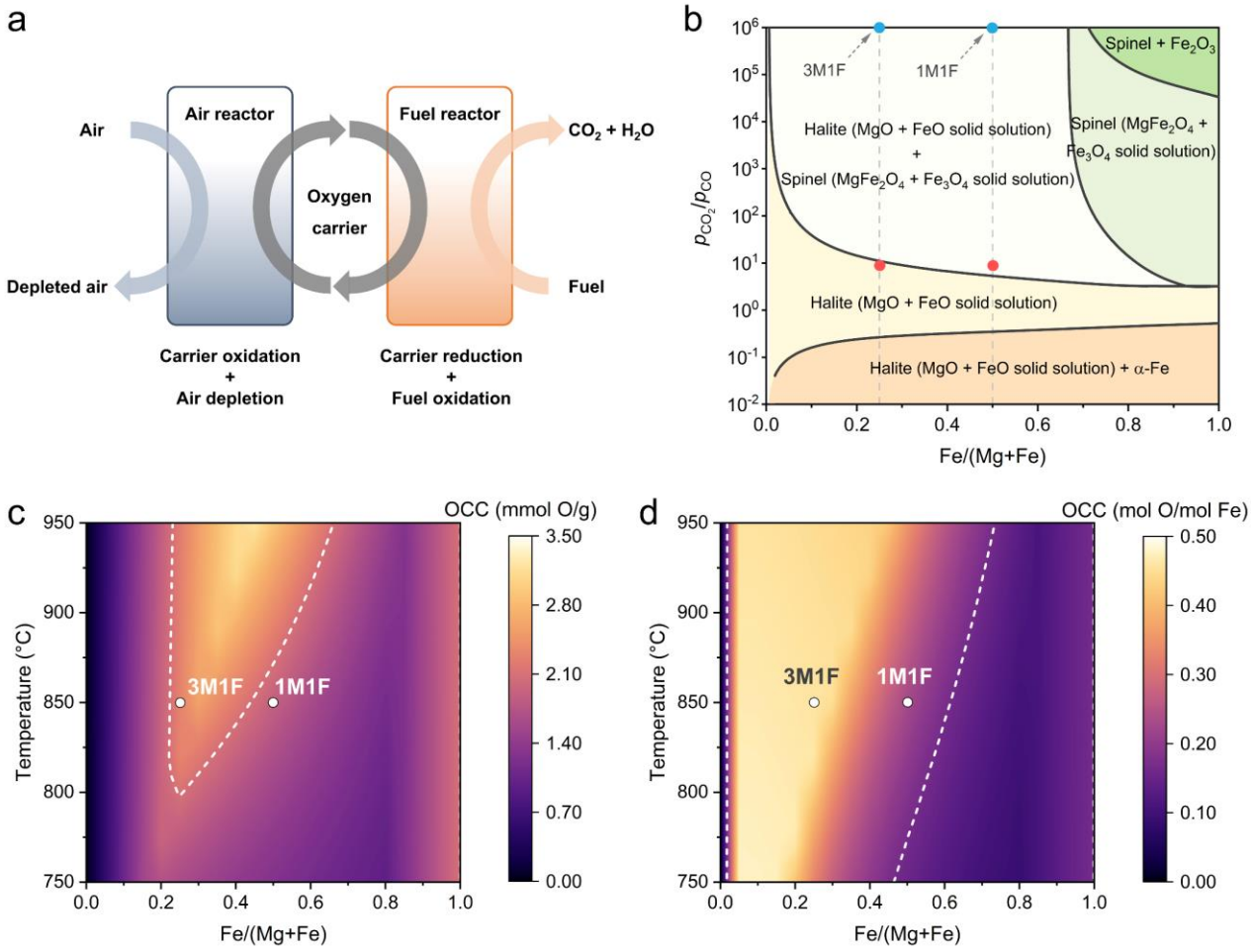

Figure 1. (a) Schematic illustrations of the chemical looping combustion concept. (b) Pressure-composition phase diagram of the Mg-Fe-O system calculated at 850 °C. Equilibrium phase compositions of the fresh and reduced (in CO_2/CO = 9:1) oxygen carriers are marked with blue and red dots, respectively. (c-d) Contour plots of the calculated OCC of Mg-Fe-O system as functions of working temperature and Fe/Mg ratio, expressed in (c) mmol oxygen atom per gram of solid and (d) mol of oxygen atom per mol of Fe present in the solid. The white dots in (c) and (d) represent the stoichiometric OCC of oxygen carriers with nominal compositions of 3M1F and 1M1F when they were subjected to CLC operation at 850 °C. The white dotted lines in (c) and (d) represent the conditions where the OCC is equivalent to that of the Fe_2O_3–Fe_3O_4 transition.

EXPERIMENTAL SECTION

Preparation of oxygen carriers

MgO and Fe_2O_3 (Sigma-Aldrich) were used as raw materials without any further purification. In a typical synthesis of 3M1F, 14.51 g (0.36 mol) of MgO and 9.58 g (0.06 mol) of Fe_2O_3 were mixed with 10 mL ethanol in a planetary ball mill (Retsch PM 100), and ball milled for 1 h at 350 rpm. The resulting products were dried in air at 80 °C overnight. The oxygen carriers were prepared by calcining the MgO-Fe_2O_3 mixture in a muffle furnace at 1100 °C (heating rate of 5 °C/min) for 30 h in air. The calcined powders were sieved to ~100 μm for characterization and CLC experiments. The same method could be applied to synthesize 1M1F, except that 4.84 g (0.12 mol) of MgO was used as Mg precursor.

Characterization of oxygen carriers

The crystal structures of the oxygen carriers were studied by powder X-ray diffraction (XRD) in a Bruker D8 Advance diffractometer with filtered Cu Kα radiation (λ = 1.5418 Å) at 40 kV and 40 mA under ambient condition. The XRD pattern were collected with 2θ range from 10°

to 90°, a step size of 0.02°, and a collection time of 1 s/step. Rietveld refinement of the diffraction data was performed using GSAS software with EXPGUI.[29] TEM images were obtained on a JEOL 2100F transmission electron microscope at 200 kV. The morphologies of the samples were examined by a field emission scanning electron microscope with energy dispersive spectroscopy (JEOL JSM-7200F). Specific surface areas were determined from nitrogen adsorption/desorption isotherms, measured on a Micromeritics 3Flex BET system. The samples were degassed in vacuum at 200 °C for 12 h before the isotherm measurements. X-ray absorption spectroscopy (XAS) was carried out under transmission mode at the XAFCA beamline of Singapore Synchrotron Light Source. Fe standard foil was used for energy calibration. The samples were mixed with BN and pressed into a pellet. Data processing was performed with the Demeter 0.9.26 software package.[30] The Fe chemical state was further studied by ^{57}Fe Mössbauer spectroscopy with ^{57}Co γ-quantum source (Rh matrix). In a typical measurement, the powdered sample was uniformly compacted with iron density of ~10 mg/cm^2. All spectra were collected at room temperature and fitted to a Lorentzian shape with a least square fitting procedure. The isomer shifts (IS) were given with respect to the centroid of α-Fe at room temperature. XPS analysis was performed using a Kratos AXIS Supra spectrometer with a monochromatic Al Kα source (1846.6 eV). The obtained XPS spectra were deconvoluted with CASA XPS software after correcting the binding energies of all the elements against the adventitious carbon C1s core level at 284.8 eV. The Raman spectra were obtained by a Renishaw inVia Reflex Raman spectrometer using an excitation wavelength of 514 nm. Thermogravimetric analysis (TGA/DSC2, Mettler Toledo) was performed to determine the lattice oxygen activity of the oxygen carrier samples through temperature programmed reduction experiments in H_2 (H_2-TPR). In a typical H_2-TPR analysis, ~20 mg of sample was first degassed by heating in N_2 from 50 °C to 200 °C at a rate of 10 °C/min, held

isothermally for 30 min, followed by a temperature ramp to 900 °C in 5 % H_2/N_2 at a rate of 5 °C/min.

Chemical looping combustion (CLC) experiments

The CLC performance of the as-prepared oxygen carriers was evaluated in an atmospheric pressure packed bed reactor externally heated by a tubular furnace (MTF 10/15/130, Carbolite). In each experiment, 200 mg of oxygen carriers were packed in an alumina tube of I.D. = 8 mm and wall thickness of ~1 mm. The packing arrangement, from top to bottom, is as follows: 5 g of white alumina sand (mean particle diameter of 2.5 mm), 0.2 g of oxygen carrier powder, 0.1 g of white alumina sand (mean particle diameter of ~0.4 mm), and a plug of quartz wool. In each redox cycle, the feed gases were, consecutively: 2 min of N_2 (purge), 10 min of 2.5 vol% CO with 22.5 vol% CO_2 balanced by N_2 (reduction), 2 min of N_2 (purge), and 5 min of 5 vol% O_2 in N_2 (oxidation). The experiments were conducted isothermally at 850 °C for 100 redox cycles, and the total gas flow rate was maintained at 200 mL/min (STP) at all times by digital mass flow controllers (CS200-A, Sevenstar). Here, a CO_2:CO ratio of 9:1 is chosen to simulate the thermodynamic environment in a typical fuel reactor having a bubbling fluidized bed condition at 850 °C. This simplistic representation of the fuel composition also simplifies the interpretation of experimental results compared to experiments using real gaseous fuels (e.g., a mixture of hydrocarbons, CO, CO_2, H_2, H_2O); the results of the latter case are typically complicated by side reactions such as water-gas-shift: $CO + H_2O \rightleftharpoons H_2 + CO_2$. The compositions of the effluent gases were measured using online gas analyzers (Caldos27, Uras26 and Magnos208, EL3020 series, ABB) at a constant sampling frequency of 1 Hz.

The flue gas concentration profiles for two consecutive redox cycles of a typical packed bed CLC experiment are shown in Figure S1. The OCC values were calculated by integrating the difference of gas mole fraction of the effluent leaving an active bed and that leaving an inert

bed in each cycle. Based on the gas species analyzed (viz. CO, CO_2 and O_2), the oxygen carrying capacities, in mmol O/g_{solid} can be calculated in three ways:

$$OCC_{CO}=\frac{N_{tot}\int_{\text{reduction period}}\left(y_{CO,blank}-y_{CO,OC}\right)dt}{m_{OC}} \quad (1)$$

$$OCC_{CO_2}=\frac{N_{tot}\int_{\text{reduction period}}\left(y_{CO_2,OC}-y_{CO_2,blank}\right)dt}{m_{OC}} \quad (2)$$

$$OCC_{O_2}=\frac{2N_{tot}\int_{\text{oxidation period}}\left(y_{O_2,blank}-y_{O_2,OC}\right)dt}{m_{OC}} \quad (3)$$

where N_{tot} is the total molar flowrate (in mol/s) of gases leaving the reactor; $y_{i,blank}$ and $y_{i,OC}$ are the gas mole fractions of species i leaving a blank bed and an active bed, respectively; m_{OC} is the mass (in gram) of the oxygen carrier used in each CLC experiment. The OCC values calculated in all three methods closely agree, suggesting excellent oxygen balance.

RESULTS AND DISCUSSION

Thermodynamic analysis

First, we computationally study the thermodynamics of the Mg-Fe-O system. The Mg-Fe-O phase diagrams were computationally generated by the CALPHAD method[31] using the MTDATA software developed by the National Physical Laboratory (NPL), UK.[32] The metal oxide database used for the calculation was also developed by NPL. Pressure-composition phase diagrams were calculated over the temperature range between 750 °C and 950 °C, which are the typical operating temperatures for CLC. The oxygen partial pressure of the system, p_{O_2} is used to compute the value of p_{CO_2}/p_{CO} in the fuel reactor according to $CO + 1/2O_2 \rightleftharpoons CO_2$. Then, p_{O_2} was varied by changing the total pressure of the closed system consisting of O, Fe and Mg atoms at a given temperature. Similar calculations were performed for Fe-O-Al_2O_3,

NaO-Fe-O-Al_2O_3[33] and CaO-Fe-O[34, 35] systems in previous studies. By reviewing the various ternary oxide phase diagrams, we found the MgO-Fe-O system to be beneficial to improving the OCC for CLC. From the pressure-composition phase diagram shown in Figure 1b, it can be observed that the phase boundaries between the corundum (Fe_2O_3) and the spinel phase, and that between the spinel (nominally Fe_3O_4) and the halite phase (nominally FeO) shift to higher p_{CO_2}/p_{CO} ratios as the MgO content in the Mg-Fe-O system increases. These upwards shifts imply that Fe^{3+} becomes easier to reduce to Fe^{2+}. The promoted reducibility may be attributed to the fact that the dissolution of Fe^{2+} into the halite solid solution shifts the equilibrium: CO + $Mg_{1-x}Fe_{2+x}O_4 \rightleftharpoons 3Mg_yFe_{1-y}O + CO_2$ to the right, favoring the release of lattice oxygen and deeper reduction. Based on the phase diagrams calculated over the temperature range of 750−950 °C, we estimated the phase compositions of the Mg-Fe-O system when it is in equilibrium with a 9:1 mixture of CO_2 and CO, which represents a typical gas composition in the fuel reactor of CLC. With the calculated equilibrium compositions, we then compute OCC, in mmol O/g_{solid} and mol O/mol Fe, of the Mg-Fe-O oxygen carriers as a function of temperature and composition, as shown in Figures 1c and 1d, respectively. From Figures 1c and 1d, we can identify an optimal region where the theoretical OCCs are higher than 2.08 mmol O/g_{solid} (or 0.167 mol O/mol Fe), which corresponds to the stoichiometric OCC of the Fe_2O_3-Fe_3O_4 transition. To validate the thermodynamic calculations, we chose the Mg/Fe ratios of 1:1 and 3:1 (denoted as 1M1F and 3M1F, with nominal phase compositions of MgO•$MgFe_2O_4$ and 5MgO•$MgFe_2O_4$, respectively) and experimentally investigated the performance of the corresponding oxygen carriers under CLC conditions at 850 °C. According to Figure 1c, the 3M1F oxygen carrier with a stoichiometric OCC of 2.28 mmol O/g_{solid} (0.45 mol O/mol Fe) falls inside the optimal region, whereas the 1M1F oxygen carrier with a stoichiometric OCC of 1.90 mmol O/g_{solid} (0.23 mol O/mol Fe), falls outside the optimal region.

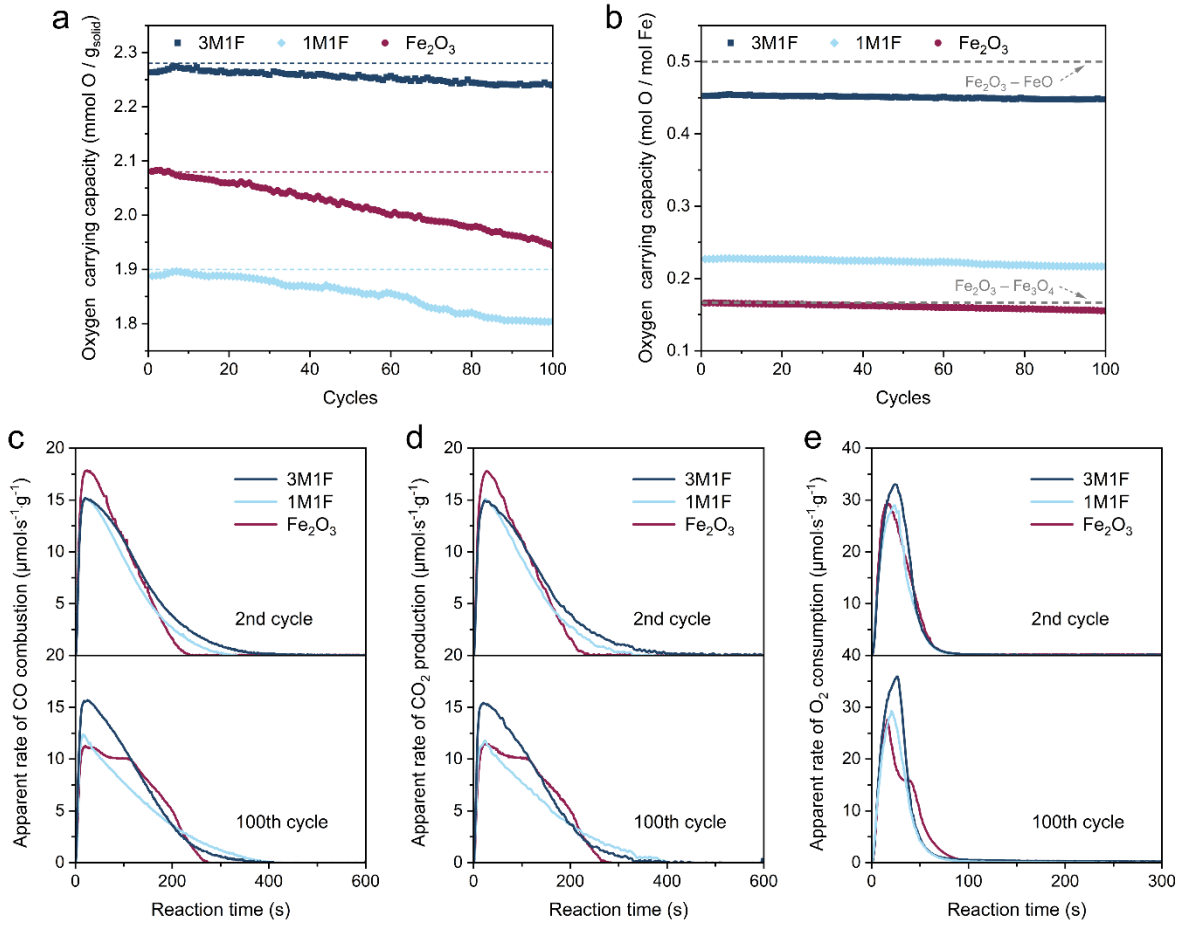

Figure 2. Oxygen carrier performance for chemical looping combustion. (a) The measured OCC per unit mass of oxygen carrier; the dashed lines represent the predicted OCC by calculated phase diagrams. (b) The measured OCC per unit number of Fe present in the oxygen carriers. Apparent rate of (c) CO combustion, (d) CO_2 production, and (e) O_2 consumption for 3M1F, 1M1F, and commercial Fe_2O_3 during the 2nd and the 100th CLC cycles.

Chemical looping combustion (CLC) experiment

The CLC performance of the 1M1F and 3M1F samples, synthesized by solid-state reaction between MgO and Fe_2O_3 precursors, was studied in a packed-bed reactor operating isothermally at 850 °C. Unmodified commercial Fe_2O_3 was also evaluated as a reference. In each redox cycle, the oxygen carrier combusts a 9:1 mixture of CO_2 and CO, followed by regeneration in 5% O_2/N_2. Complete CO combustion could be observed, whilst the reduced

oxygen carrier was rapidly regenerated when exposed to oxygen, manifesting satisfactory redox activity (see Figure S1 for an example of the gas concentration profile during a CLC experiment). From the gas concentration profiles, the OCC of the oxygen carriers were calculated and plotted over redox cycles in Figure 2a. Although the unreducible MgO takes up 60 wt% of the material, the measured OCC of 3M1F was 2.26 mmol O/g, closely agreeing with the predicted OCC of 2.28 mmol O/g. The OCC of 1M1F is also consistent with the calculated value of 1.89 mmol O/g. Both results suggest the reliability of the computational method to predict OCCs. When the OCCs are represented on molar basis (Figure 2b), it can be seen that 3M1F carries 0.45 mol O/mol Fe, i.e., nearly all the Fe^{3+} can be reduced to Fe^{2+} in the fuel reactor; this is equivalent to a full transition from Fe_2O_3 to FeO. From a thermodynamic point of view, only 1/3 of the Fe^{3+} in pure Fe_2O_3 can be reduced to Fe^{2+} (i.e., the Fe_2O_3 – Fe_3O_4 transition with an OCC of 0.167 mol O/mol Fe) under identical conditions. In comparison, the reducibility of 1M1F was between that of Fe_2O_3 and 3M1F, showing an experimental OCC of ~ 0.23 mol O/mol Fe. Therefore, it is apparent that MgO doping could practically enhance the reducibility of Fe. In the case of 3M1F, the enhancement in reducibility overcomes the dilution by MgO, resulting in an overall improvement in the OCC on a gravimetric basis.

Figure 2a also shows that the introduction of Mg improves the redox cycling stability of the Fe-based oxygen carriers. 3M1F exhibits a relatively consistent OCC of 2.26 mmol O/g over 100 consecutive CLC cycles. For 1M1F, a 5% drop in OCC was observed over 100 cycles. In contrast, unmodified commercial Fe_2O_3 suffers from a serious capacity decay, losing 6.7% of its initial OCC after 100 cycles. The effect of MgO addition on the reaction kinetics of the Fe-based oxygen carriers is examined by comparing the apparent rates of reduction and oxidation of 3M1F and 1M1F during the packed bed CLC experiment against those of the commercial Fe_2O_3 oxygen carrier, as shown in Figures 2c, 2d and 2e. From the comparison, it is clear that the two Mg-doped oxygen carriers showed comparable reaction rates in the second cycle, with

maximum rates of 15 μmol s^{-1} g^{-1} and 30~34 μmol s^{-1} g^{-1} during the reduction and the oxidation stages, respectively; these maximum values are slightly slower and faster than those for the reduction and oxidation of commercial Fe_2O_3 (i.e., 18 μmol s^{-1} g^{-1} and 30 μmol s^{-1} g^{-1}) respectively. Given that 3M1F and 1M1F nominally contain 40 wt% and 67 wt% of Fe_2O_3, respectively, it can be inferred that the addition of MgO has little impact on the overall activity of the Fe-based oxygen carriers (using commercial Fe_2O_3 as a benchmark). In fact, on a per Fe atom basis, the oxygen carrier would be more active after MgO doping. By the 100th cycle, the apparent rate of reduction of commercial Fe_2O_3 (corresponding to the reaction in the fuel reactor) has notably decreased, showing a maximum rate of ~11 μmol s^{-1} g^{-1}, which corroborates its cyclically decaying OCC, as shown in Figure 2a. For 3M1F, the reaction rates during the oxidation stage and the reduction stage remain largely unchanged over 100 cycles, with signs of marginal reduced kinetics in the 100th cycle cf. the 2nd cycle. For 1M1F, there is a slight decrease in the rate of reaction of the first 100 s of the reduction stage. Interestingly, for all three samples, the apparent rates of oxidation (Figure 2e) in the 100th cycle are virtually identical to those in the 2nd cycle, suggesting that the capacity-limiting step in the CLC experiments is the reduction stage. By evaluating the morphologies of the oxygen carriers before and after CLC cycles by SEM and BET analysis (Figures 3d, 3e and S3; Table S3), it is found that the deactivation of the oxygen carriers over CLC cycles is correlated to the loss of surface area and porosity. Without MgO doping, unmodified Fe_2O_3 suffers greatly from sintering (Figures S3b). In comparison, 1M1F and 3M1F appear more resistant to sintering (Figures S3e and S3h) and maintained a considerable portion of their initial surface area over 100 redox cycles (Table S3). We further subjected the oxygen carriers to 250 redox cycles under identical reaction conditions (i.e., with a total experimental duration of 79 h), with the cyclic OCC results and the characterization of the cycled oxygen carriers (by SEM and BET) shown in Figures S2, S3c, S3f, and S3i, and Table S3, respectively. Indeed, 3M1F shows the

most cyclically stable oxygen carrying performance over 250 CLC cycles, whilst appearing to be the most sintering resistant. In contrast, the Mg-free Fe_2O_3 sample shows the most severe sintering and the worst cyclic stability, with its gravimetric OCC dropping below that of 1M1F after around 190 cycles. Therefore, the results above unambiguously indicate that MgO doping could substantially promote both the oxygen carrying capacity and the cycling stability of Fe-based oxygen carriers, whilst insignificantly impacting the reaction kinetics.

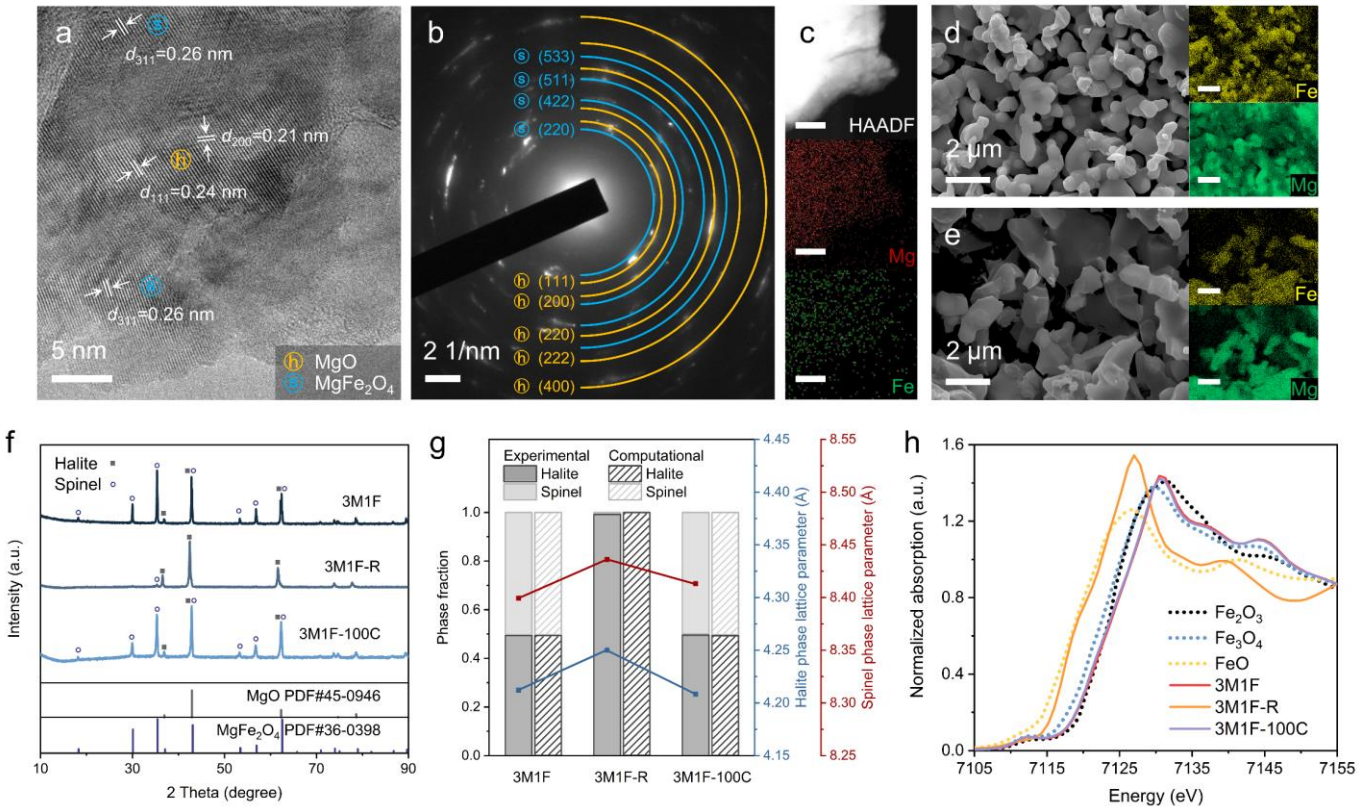

Figure 3. Phase and chemical state analysis of 3M1F oxygen carriers at various stages of the redox cycles. (a) HR-TEM and (b) corresponding SAED images. (c) HAADF-STEM image and EDX elemental maps. SEM images and EDX elemental maps of (d) 3M1F and (e) 3M1F-100C. (f) XRD patterns and (g) Phase fractions and lattice parameters estimated from the Rietveld refinement of the XRD data. (h) Normalized Fe K-edge XANES spectra of the oxygen carriers and Fe_2O_3, Fe_3O_4, and FeO standards. Scale bar: (c) 50 nm, (d) 2 μm.

Structural evolutions and reaction mechanism

To elucidate the origin of the significantly improved CLC performance of 3M1F, the physical and chemical evolution of the 3M1F oxygen carriers over redox cycles was experimentally investigated. Specifically, the sample when it is freshly prepared (3M1F), reduced in the first cycle (3M1F-R), and fully regenerated after 100 CLC cycles (3M1F-100C), was characterized using complementary experimental techniques.

First, the reducibility of the oxygen carrier samples was characterized by H_2-TPR, as shown in Figure S4. In general, TPR peaks at lower temperatures (i.e., < 600 °C) correspond to highly active lattice oxygen, which are generally considered to be relevant to CLC, whereas the TPR peaks at higher temperatures (i.e., > 600 °C) correspond to lattice oxygen that are generally regarded as more suitable for partial oxidation of hydrocarbons (i.e., chemical looping reforming). For Fe_2O_3, the three TPR peaks correspond to the Fe_2O_3 – Fe_3O_4 (~ 400 °C), Fe_3O_4 – FeO (~ 650 °C) and FeO – Fe (~ 850 °C) transitions, respectively. For 3M1F, two reduction peaks at ~600 and ~800°C could be observed, which are assigned to the Fe^{3+} – Fe^{2+} and Fe^{2+} – Fe^0 transitions, respectively. Compared to the stepwise reduction of Fe_2O_3, the mixed solid solution in 3M1F oxygen carrier enables a complete transition of Fe^{3+} to Fe^{2+} at a lower temperature, suggesting that significantly more lattice oxygen could be utilized for CLC. After reduction in a 9:1 mixture of CO_2 and CO, 3M1F-R shows only a high temperature TPR peak ascribed to the reduction of Fe^{2+} to metallic Fe. The absence of any notable TPR peak below 600 °C verifies that all the Fe^{3+} has been completely reduced to Fe^{2+}. These results clearly indicate the promoted lattice oxygen activities of the 3M1F oxygen carrier.

X-ray diffraction (XRD) patterns (Figure 3f) show that fresh 3M1F consists of a mixture of MgO (halite) and $MgFe_2O_4$ (spinel), in complete agreement with the computational prediction (Figure 1b). High resolution transmission electron microscopy (HR-TEM), and selected area electron diffraction (SAED) and energy dispersive X-ray (EDX) analyses (Figures 3a-3c) showed that the MgO halite phase and $MgFe_2O_4$ spinel phase are finely mixed at ~10 nm scales,

while the Mg and Fe elements were uniformly dispersed across the sample. The SEM-elemental mapping of the samples before and after CLC cycles (Figures 3d and 3e) also confirms the absence of any irreversible phase segregation. The successful synthesis of 3M1F with the target composition of $5MgO•MgFe_2O_4$ is confirmed by the results of quantitative Rietveld refinement (Figure 3g and Table S4). The lattice parameters of the cubic halite and spinel phases of the freshly calcined 3M1F are estimated to be 4.21 Å and 8.40 Å, respectively, agreeing well with the reference MgO (ICSD-26958) and $MgFe_2O_4$ (ICSD-158107) structures. Upon reduction, both phases underwent lattice expansion, which is attributed to the reduction from Fe^{3+} (ionic radius = 0.64 Å) to Fe^{2+} (ionic radius = 0.78 Å). The phase composition and the lattice parameters of 3M1F after 100 redox cycles (3M1F-100C) are almost identical to those of fresh 3M1F, indicating excellent structural reversibility, agreeing with the excellent cyclic stability shown in Figure 2.

The electronic structures and the coordination environments of the Fe species in the 3M1F oxygen carrier are probed by X-ray absorption spectroscopy (XAS). The Fe K-edge XANES of the oxygen carriers at various stages of redox cycling are shown in Figure 3h. The white line of fresh 3M1F is close to that of the Fe_2O_3 reference, confirming that all Fe species have an oxidation state of +3. However, the features of the extended edge of fresh 3M1F show closer resemblance to the Fe_3O_4 reference, i.e., the Fe^{3+} are in a spinel structure (viz. $MgFe_2O_4$). Upon reduction in a 9:1 mixture of CO_2 and CO, the Fe K-edge of the reduced oxygen carrier (3M1F-R) moved to the left of the Fe_3O_4 reference, overlapping with the adsorption edge of the FeO reference, signifying the complete reduction to $Mg_{1-x}Fe_xO$. Similar to the XRD results, the oxidized oxygen carriers after 100 redox cycles (3M1F-100C) show adsorption edges that are virtually identical to the fresh 3M1F, suggesting cyclic reversibility

In spinel structures, the coordination environments of the metal centers (Mg^{2+}, Fe^{2+} and Fe^{3+}) depend on the occupancies of the tetrahedral (A) and octahedral (B) sites, as depicted in Figure

4a. In the fully oxidized 3M1F, the site occupancies of $MgFe_2O_4$ can also be described by the degree of inversion, x, i.e., $(Mg_{1-x}Fe_x)_A(Mg_xFe_{2-x})_BO_4$.[36] When $x = 0$, all Mg^{2+} occupy tetrahedral sites, adapting a normal spinel structure, whereas $x = 1$ implies all Mg^{2+} occupy octahedral sites, adapting an inverse spinel structure. Therefore, spectroscopic techniques were used to elucidate the site occupancies in relation to the oxidation states of Fe in the spinel solid solution during chemical looping combustion.

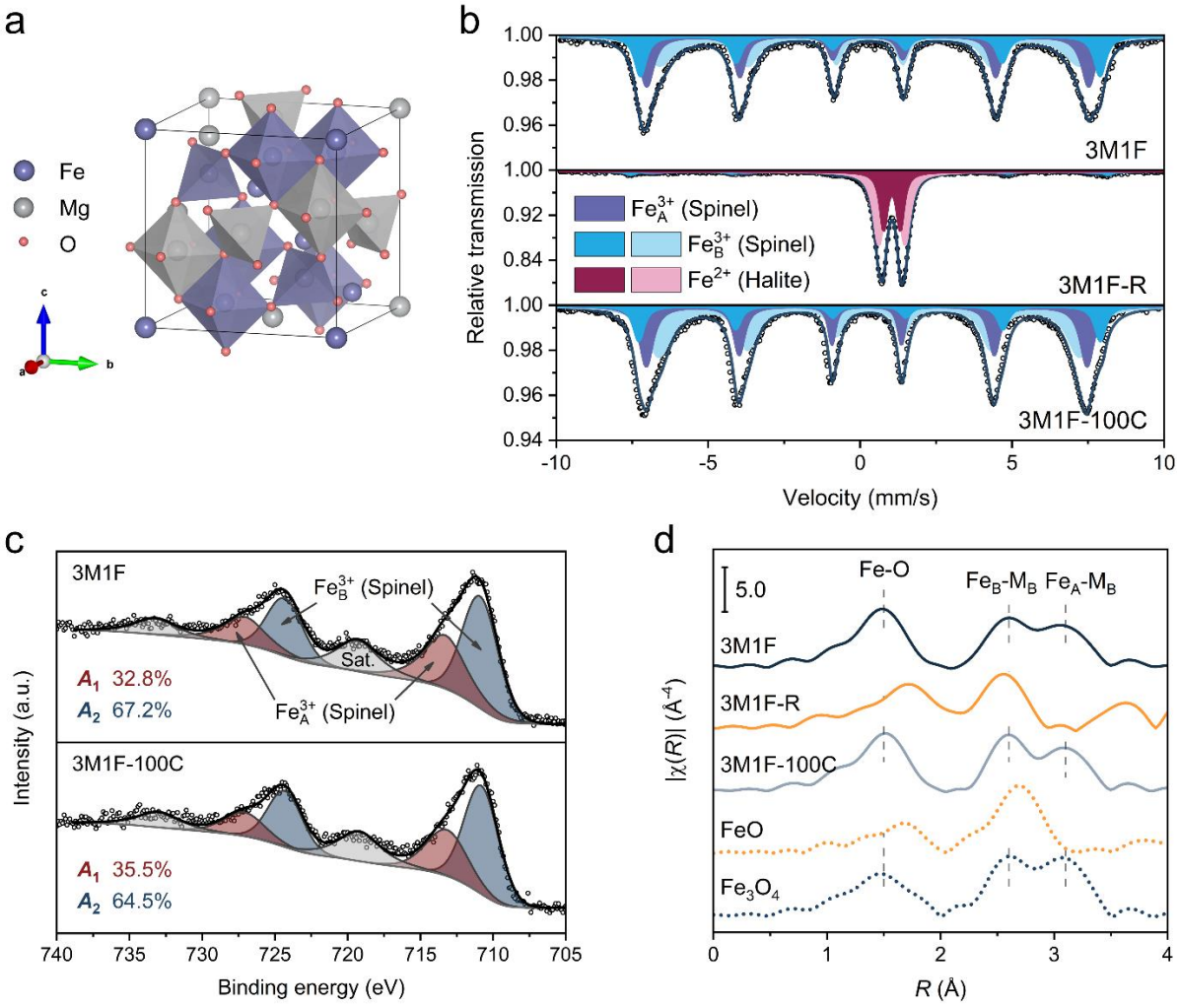

Figure 4. Determination of the cation distribution in the magnesium ferrite spinel. (a) Crystal structure of the mixed spinel, with Mg and Fe occupying both the tetrahedral and octahedral sites. Some oxygen atoms have been omitted for clarity. (b) Mössbauer spectra. (c) Fe 2p XPS spectra. (d) Fourier transform of the Fe K-edge EXAFS spectra of the oxygen carriers at various stages of the redox cycles.

^{57}Fe Mössbauer spectra were measured to probe the coordination environments of the Fe species in the oxygen carrier under different conditions. Based on the fitted Mössbauer spectra (Figure 4b, also see quantification in Table 1), only trivalent Fe^{3+} cations confined in the spinel structure can be identified in fresh 3M1F. The Fe^{3+} occupying octahedral sites (B sites) exhibits two types of hyperfine field responses (viz. H ~ 47 T and ~ 43 T), which was attributed to slightly different chemical environment of Fe cations (number of surrounding Mg differs). Overall, the percentage of Fe cations occupying A and B site are calculated to be 34% and 66%, respectively, which approximately correspond to a $(Mg_{1/3}Fe_{2/3})_A(Mg_{2/3}Fe_{4/3})_BO_4$ structure. In other words, the site occupancies by Fe and Mg are entirely random and proportional to the Mg:Fe ratio in $MgFe_2O_4$ spinel. After reduction, 3M1F-R primarily consists of Fe^{2+} (90 mol%) occupying octahedral centers in the halite phase while only 10% unreduced Fe^{3+} remains; these results are in good agreement with the quantifications obtained by the packed bed experiments and XANES analysis. For 3M1F-R, the two different quadrupole shift values (viz. 0.55 and 0.87 mm/s) for Fe^{2+} in the halite solid solution are attributed to different Mg neighborhoods, which arises from the local variations in cationic compositions that are commonly observed in solid solutions.

Table 1. Mössbauer spectra fitting results, showing the distribution of different Fe species in the tetrahedral (A) and octahedral (B) sites in spinel and halite phases.

Sample	IS (mm/s)	QS (mm/s)	H (T)	A (%)	*x**	Assignment
3M1F	0.25	-	45.2	34	0.68	Fe^{3+}-A site of spinel
	0.31	-	47.0	23		Fe^{3+}-B site of spinel

	0.31	-	42.9	43		Fe^{3+}-B site of spinel		
3M1F-100C	0.22	-	45.1	33	0.66	Fe^{3+}-A site of spinel		
	0.31	-	47.2	16		Fe^{3+}-B site of spinel		
	0.30	-	43.0	51		Fe^{3+}-B site of spinel		
3M1F-R	1.04	0.55	-	33	-	Fe^{2+} in MgO		
	1.04	0.87	-	57				
	0.31	-	48.8	5		Fe^{3+} in spinel		
	0.46	-	45.3	5				

IS: isomer shift, QS: quadrupole shift, H: hyperfine field. *For 3M1F-R, the signal associated with the spinel phase is too weak to provide a reliable estimate of its site occupancy.

Fe 2p XPS (Figure 4c) is also analyzed to determine the degree of inversion of the spinel ferrites at the surface region. Fe^{3+} that occupy the tetrahedral sites produce 2p peaks with a higher binding energy (727.1 eV and 713.0 eV for 2p1/2 and 2p3/2, respectively) than those occupying the octahedral sites (724.3 eV and 710.9 eV for 2p1/2 and 2p3/2, respectively).[37] Accordingly, the Fe 2p peaks are deconvoluted to determine the relative site occupancies and therefore the values of x. For 3M1F, 32.8% Fe^{3+} occupy tetrahedral sites, which translates to x = 0.66 for 3M1F. Using the same analysis, x is found to be 0.71 for 3M1F-100C. The site occupancies of the spinel phase by Mg^{2+}, as shown by the deconvoluted Mg 2p XPS (Figure S7), are in qualitative agreement with the analysis of the Fe 2p XPS. For 3M1F-R, only one peak corresponding to Mg^{2+} in the halite phase could be fitted, suggesting the absence of any spinel phase. Therefore, the structure and composition of the oxide phases in the surface region of the oxygen carriers (measured by XPS), are the same as those in the bulk (measured by Mössbauer spectroscopy).

The structures of the solid solution phases in the 3M1F oxygen carrier are further verified by extended X-ray absorption fine structure (EXAFS) analysis, as shown by the k^3-weighted Fourier transforms (FTs) of the EXAFS spectra shown in Figure 4d. The characteristic peaks of the spinel structure can be seen for 3M1F, 3M1F-100C and the Fe_3O_4 reference: the first peak near 1.5 Å is assigned to the Fe_A-O and Fe_B-O bonds; the second peak at ~2.6 Å corresponds to the first iron-metal shell (Fe_B-M_B), where the Fe and the metal belong to two edge-sharing octahedra. The peak with $R > 3$ Å is assigned to the scattering pair between a tetrahedral Fe center and a corner-sharing octahedral-center in the spinel structure, in which at least one of the metal centers is Fe^{3+} or Fe^{2+}.[38] For 3M1F-R, the two main EXAFS peaks at 1.7 Å and 2.5 Å could be ascribed to the Fe-O bonds of the FeO_6 octahedra and the Fe-Fe/Mg distance between neighboring octahedra in the halite solid solution, respectively, similar to that of the FeO reference. Fitting of the EXAFS data (Figure S8) suggests that occupancies of 1/3 and 2/3 for the tetrahedral (A) and octahedral (B) sites by Fe, respectively (Table S5) could explain the EXAFS data well, in close agreement with the Mössbauer spectroscopy and XPS results. In addition, 3M1F exhibits similar EXAFS before and after CLC cycles, i.e., the structure of the solid solution-based oxygen carrier is entirely regenerable.

Results from Raman measurements (Figure S9) are also in agreement with the above-mentioned experimental evidence, where peak splitting could be observed due to mixed occupancies by Mg^{2+} and Fe^{3+} in both the tetrahedral and octahedral sites. To conclude, the present experimental evidence suggests that $MgFe_2O_4$ forms a random spinel structure, which is in principle thermodynamically less stable (i.e., more reactive) than the ordered Fe_3O_4 inverse spinel.

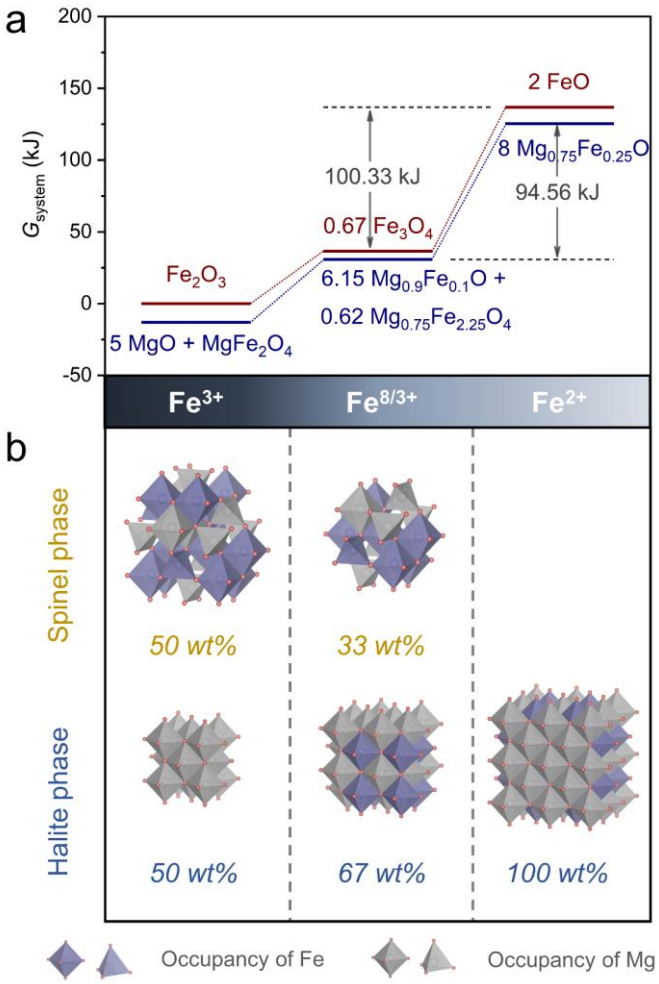

Figure 5. (a) Gibbs free energy diagram of the stepwise reduction of Fe_2O_3 and 3M1F, and (b) the corresponding phase compositions in this process.

Based on the experimental results, we conclude the underlying reason for the improved lattice oxygen activity of 3M1F. For Fe_3O_4, the thermodynamically stable inverse spinel structure makes the reduction from Fe^{3+} to Fe^{2+} exergonically demanding. The addition of MgO result in the formation of a spinel solid solution with randomized site occupancies. Such structural disorder destabilizes the spinel phase as well as making the Fe^{3+} in the spinel more reducible. In other words, the lattice oxygen of the MgO-doped spinel phase becomes more active. Such promotional effect could boost the OCC of 3M1F beyond the stoichiometric maximum of the Fe_2O_3/Fe_3O_4 redox couple. This structural-activity relationship is also

corroborated by the computational thermodynamic calculations using MTDATA, as shown in Figure 5a. Starting from 100% Fe^{3+} (which corresponds to Fe_2O_3 in the case of a Mg-free system), 3M1F would first form a mixture of $Mg_{0.75}Fe_{2.25}O_4$ solid solution and $Mg_{0.9}Fe_{0.1}O$ halite solid solution, with a Fe^{3+}:Fe^{2+} ratio of 2:1 (i.e., equivalent to Fe_3O_4 in a Mg-free system). At this stage, the promotional effect by MgO is not obvious. Nevertheless, the reduction from 100% Fe^{3+} to a 2:1 mixture of Fe^{3+} and Fe^{2+} is thermodynamically facile in a typical fuel reactor environment and generally has little impact on the cyclic OCC. The subsequent reduction from a 2:1 mixture of Fe^{3+} and Fe^{2+} to 100% Fe^{2+}, which is more relevant to enhancing the OCC in a fuel reactor, requires 94.56 kJ. In comparison, the equivalent transition from Fe_3O_4 to FeO is more exergonic and requires 100.33 kJ. The computationally predicted trend in reducibility versus oxidation states is also in agreement with the H_2-TPR results shown in Figure S4. Thus, from a thermodynamic point of view, the incorporation of Mg to the Fe-based oxygen carrier formulation could fundamentally promote the reducibility of Fe^{3+} to Fe^{2+} during CLC.

In each CLC cycle, 3M1F is cycled between a halite-spinel phase mixture and a single halite solid solution, as depicted in Figure 5b. Starting with a mixture of spinel ($MgFe_2O_4$) and halite (MgO), the 3M1F oxygen carrier gradually supplies lattice oxygen to the combustion of carbonaceous fuels, resulting an enrichment of Fe^{2+}. The enrichment of divalent metal cations destabilizes the spinel phase, which subsequently transforms into the halite phase. The transition is accompanied by a net migration of Fe^{2+} and Mg^{2+} from $Mg_{1-y}Fe_{2+y}O_4$ to $Mg_{1-x}Fe_xO$. As the reduction continues, the oxygen carrier becomes depleted of spinel phase and Fe^{3+}, eventually forming a halite phase with a nominal composition of $Mg_{0.75}Fe_{0.25}O$. During the oxidation half-cycle, the phase transition is reversed, as more halite phases transforms into the spinel $Mg_{1-y}Fe_{2+y}O_4$ solid solution, eventually restoring the fully oxidized state of $5MgO•MgFe_2O_4$. Throughout the redox cycling, there is no precipitation of any tertiary solid phase, which is commonly observed during the chemical looping of conventional mixed oxide

oxygen carriers. The absence of a multi-phase mixture may also be beneficial to the cyclic stability, as accumulative phase segregation over redox cycles can be avoided.[39, 40] Lastly, it should be noted that the evolution of oxygen carriers as a function of phase composition and reaction conditions is deduced based on computational calculations and ex situ characterization results. In future studies, more direct experimental evidence could be provided by in situ characterization techniques, such as in situ XRD and in situ XAS, to validate the findings in the present work.

In addition to being a promoter, MgO with a high Tammann temperature of 1290 °C also acts as a supporting material,[41] which significantly increased the sintering resistance of the 3M1F oxygen carrier, sustaining its porous morphology and subsequently its experimentally accessible OCC, as shown by the cycling experiments (Figures 2a, 2b and S3). Nevertheless, the continued decay in activities of the 3M1F oxygen carrier over prolonged CLC experiment should be addressed in future work, e.g., by further optimizing the Mg:Fe ratio or incorporating other support materials, such as ZrO_2.[42]

We also remind the readers that the gaseous fuel used in the present study (i.e., a 9:1 mixture of CO_2 and CO, balanced by N_2) only simulates the thermodynamic conditions in a bubbling fluidized bed reactor and with a significantly simplified composition compared to those used in real CLC systems for the ease of result interpretation. To further verify the suitability of the 3M1F oxygen carrier in practical applications, the phase changes of the 3M1F oxygen carrier during its interaction with more realistic fuel compositions (e.g., mixtures of CH_4, CO, CO_2, H_2, H_2O, other volatile hydrocarbons and possibly sulfur compounds) should be examined in the future. Additionally, the potential enhancement in oxygen carrying capacity when 3M1F is cycled in other reactor configurations (e.g., counter current moving beds) should be investigated.

CONCLUSION

By using a simple ball-milling assisted solid-state reaction, we have successfully synthesized oxygen carriers with nominal compositions of $MgO•MgFe_2O_4$ (1M1F) and $5MgO•MgFe_2O_4$ (3M1F), both function in the form of mixtures of a halite solution ($Mg_{1-x}Fe_xO$) and a spinel ($Mg_{1-y}Fe_{2+y}O$) solid solution. This novel formulation is developed with a hypothesis-driven synthesis method, leveraging on computationally calculated phase diagrams (CALPHAD). The computationally predicted OCC are verified by CLC experiments in a packed bed, showing an OCC of 1.89 mmolO/g (0.23 mmolO/molFe) and 2.26 mmol O/g (0.45 mmol O/mol Fe) for 1M1F and 3M1F over 100 cycles, respectively. In particular, the OCC of 3M1F exceeds the widely accepted stoichiometric limit of 2.08 mmol O/g (0.167 mol O/mol Fe) of the Fe_2O_3/Fe_3O_4 redox couple. In essence, the formation of the highly disordered $(Mg_{1/3}Fe_{2/3})_A(Mg_{2/3}Fe_{4/3})_BO_4$ solid solution has substantially reduced the thermodynamic stability of the spinel phase, while the $Mg_xFe_{1-x}O$ solid solution improves the tendency to form Fe^{2+} in the product halite phase. As a result, the reducibility of Fe^{3+}, which governs the lattice oxygen activity suitable for CLC, is greatly enhanced. Most importantly, this promotion strategy does not sacrifice OCC (on a mass basis) for cyclic stability or reactivity, making it superior to conventional oxygen carrier designs. In addition, the present study presents a computer-aided oxygen carrier design approach that can significantly accelerate the search for optimal oxygen carrier formulations. Such approach may be versatilely adapted as a general methodology for the high-throughput screening of novel material formulations for a variety of chemical and energy applications.

ASSOCIATED CONTENT

Supporting Information: Calculated OCC of Mg-Fe mixed oxides at temperature range of 750-950 °C, measured OCC over 250 CLC cycles, additional sample characterization results (BET surface area, XRD refinement, H_2-TPR, EXAFS fitting, SEM, XPS and Raman spectra).

Notes

The authors declare no competing financial interest.

ACKNOWLEDGMENT

The authors would like to thank the financial support by Ministry of Education Singapore's Academic Research Fund Tier 1 (RT03/19 and RG112/18) and the National Research Foundation (NRF), Prime Minister's Office, Singapore under its Campus for Research Excellence and Technological Enterprise (CREATE) programme. Y. Dai is grateful for the financial support from the National Natural Science Foundation of China (21802070).

REFERENCES

1. Romeo, L. M.; Bolea, I.; Escosa, J. M., Integration of power plant and amine scrubbing to reduce CO2 capture costs. *Applied Thermal Engineering* **2008,** *28* (8-9), 1039-1046.
2. Wappel, D.; Gronald, G.; Kalb, R.; Draxler, J., Ionic liquids for post-combustion CO2 absorption. *International Journal of Greenhouse Gas Control* **2010,** *4* (3), 486-494.
3. Smith, K. H.; Anderson, C. J.; Tao, W.; Endo, K.; Mumford, K. A.; Kentish, S. E.; Qader, A.; Hooper, B.; Stevens, G. W., Pre-combustion capture of CO2—Results from solvent absorption pilot plant trials using 30 wt% potassium carbonate and boric acid promoted potassium carbonate solvent. *International Journal of Greenhouse Gas Control* **2012,** *10*, 64-73.
4. Dai, Z.; Deng, L., Membrane absorption using ionic liquid for pre-combustion CO2 capture at elevated pressure and temperature. *International Journal of Greenhouse Gas Control* **2016,** *54*, 59-69.
5. Castillo, R., Thermodynamic analysis of a hard coal oxyfuel power plant with high temperature three-end membrane for air separation. *Applied Energy* **2011,** *88* (5), 1480-1493.
6. Stanger, R.; Wall, T., Sulphur impacts during pulverised coal combustion in oxy-fuel technology for carbon capture and storage. *Progress in Energy and Combustion Science* **2011,** *37* (1), 69-88.
7. Ishida, M.; Zheng, D.; Akehata, T., Evaluation of a chemical-looping-combustion power-generation system by graphic exergy analysis. *Energy* **1987,** *12* (2), 147-154.
8. Kvamsdal, H. M.; Jordal, K.; Bolland, O., A quantitative comparison of gas turbine cycles with CO2 capture. *Energy* **2007,** *32* (1), 10-24.
9. Lyngfelt, A., Chemical-looping combustion of solid fuels–status of development. *Applied Energy* **2014,** *113*, 1869-1873.

10. Adanez, J.; Abad, A., Chemical-looping combustion: Status and research needs. *Proceedings of the Combustion Institute* **2019,** *37* (4), 4303-4317.
11. Zafar, Q.; Mattisson, T.; Gevert, B., Integrated hydrogen and power production with CO2 capture using chemical-looping reforming-redox reactivity of particles of CuO, Mn2O3, NiO, and Fe2O3 using SiO2 as a support. *Industrial & Engineering Chemistry Research* **2005,** *44* (10), 3485-3496.
12. Tian, X.; Zheng, C. H.; Li, F. X.; Zhao, H. B., Co and Mo Co-doped Fe2O3 for Selective Ethylene Production via Chemical Looping Oxidative Dehydrogenation. *Acs Sustainable Chemistry & Engineering* **2021,** *9* (23), 8002-8011.
13. Moghtaderi, B., Application of Chemical Looping Concept for Air Separation at High Temperatures. *Energy & Fuels* **2010,** *24* (1), 190-198.
14. Jiang, B.; Li, L.; Bian, Z.; Li, Z.; Othman, M.; Sun, Z.; Tang, D.; Kawi, S.; Dou, B., Hydrogen generation from chemical looping reforming of glycerol by Ce-doped nickel phyllosilicate nanotube oxygen carriers. *Fuel* **2018,** *222*, 185-192.
15. Imtiaz, Q.; Armutlulu, A.; Donat, F.; Naeem, M. A.; Muller, C. R., Preventing Agglomeration of CuO-Based Oxygen Carriers for Chemical Looping Applications. *Acs Sustainable Chemistry & Engineering* **2021,** *9* (17), 5972-5980.
16. Hu, J.; Galvita, V. V.; Poelman, H.; Marin, G. B., Advanced chemical looping materials for CO2 utilization: a review. *Materials* **2018,** *11* (7), 1187-1219.
17. Lyngfelt, A., Chemical Looping Combustion: Status and Development Challenges. *Energy & Fuels* **2020,** *34* (8), 9077-9093.
18. Bayham, S. C.; Tong, A.; Kathe, M.; Fan, L. S., Chemical looping technology for energy and chemical production. *Wiley Interdisciplinary Reviews: Energy and Environment* **2016,** *5* (2), 216-241.
19. Tang, M.; Xu, L.; Fan, M., Progress in oxygen carrier development of methane-based chemical-looping reforming: A review. *Appl. Energy* **2015,** *151*, 143-156.
20. Imtiaz, Q.; Hosseini, D.; Müller, C. R., Review of oxygen carriers for chemical looping with oxygen uncoupling (CLOU): thermodynamics, material development, and synthesis. *Energy Technology* **2013,** *1* (11), 633-647.
21. Zafar, Q.; Mattisson, T.; Gevert, B., Redox investigation of some oxides of transition-state metals Ni, Cu, Fe, and Mn supported on SiO2 and MgAl2O4. *Energy & Fuels* **2006,** *20* (1), 34-44.
22. Chen, S.; Xiang, W.; Xue, Z.; Sun, X., Experimental investigation of chemical looping hydrogen generation using iron oxides in a batch fluidized bed. *Proceedings of the Combustion Institute* **2011,** *33* (2), 2691-2699.
23. De Vos, Y.; Jacobs, M.; Van Driessche, I.; Van der Voort, P.; Snijkers, F.; Verberckmoes, A., Processing and characterization of Fe-based oxygen carriers for chemical looping for hydrogen production. *International Journal of Greenhouse Gas Control* **2018,** *70*, 12-21.
24. De Vos, Y.; Jacobs, M.; Van Der Voort, P.; Van Driessche, I.; Snijkers, F.; Verberckmoes, A., Sustainable iron-based oxygen carriers for Chemical Looping for Hydrogen Generation. *international journal of hydrogen energy* **2019,** *44* (3), 1374-1391.
25. Kosaka, F.; Hatano, H.; Oshima, Y.; Otomo, J., Iron oxide redox reaction with oxide ion conducting supports for hydrogen production and storage systems. *Chemical Engineering Science* **2015,** *123*, 380-387.
26. Hu, J.; Poelman, H.; Marin, G. B.; Detavernier, C.; Kawi, S.; Galvita, V. V., FeO controls the sintering of iron-based oxygen carriers in chemical looping CO2 conversion. *Journal of CO2 Utilization* **2020,** *40*, 101216-101222.

27. Ghoniem, A. F.; Zhao, Z.; Dimitrakopoulos, G., Gas oxy combustion and conversion technologies for low carbon energy: Fundamentals, modeling and reactors. *Proceedings of the Combustion Institute* **2019,** *37* (1), 33-56.
28. Luo, S.; Zeng, L.; Fan, L.-S., Chemical looping technology: oxygen carrier characteristics. *Annual review of chemical and biomolecular engineering* **2015,** *6*, 53-75.
29. Toby, B. H., EXPGUI, a graphical user interface for GSAS. *Journal of applied crystallography* **2001,** *34* (2), 210-213.
30. Ravel, B.; Newville, M., ATHENA, ARTEMIS, HEPHAESTUS: data analysis for X-ray absorption spectroscopy using IFEFFIT. *Journal of synchrotron radiation* **2005,** *12* (4), 537-541.
31. Lukas, H.; Fries, S. G.; Sundman, B., *Computational thermodynamics: the Calphad method*. Cambridge university press: 2007.
32. Davies, R.; Dinsdale, A.; Gisby, J.; Robinson, J.; Martin, a. M., MTDATA-thermodynamic and phase equilibrium software from the national physical laboratory. *Calphad* **2002,** *26* (2), 229-271.
33. Liu, W.; Ismail, M.; Dunstan, M. T.; Hu, W.; Zhang, Z.; Fennell, P. S.; Scott, S. A.; Dennis, J., Inhibiting the interaction between FeO and Al 2 O 3 during chemical looping production of hydrogen. *Rsc Advances* **2015,** *5* (3), 1759-1771.
34. Ismail, M.; Liu, W.; Dunstan, M. T.; Scott, S. A., Development and performance of iron based oxygen carriers containing calcium ferrites for chemical looping combustion and production of hydrogen. *International Journal of Hydrogen Energy* **2016,** *41* (7), 4073-4084.
35. Chan, M. S.; Liu, W.; Ismail, M.; Yang, Y.; Scott, S. A.; Dennis, J. S., Improving hydrogen yields, and hydrogen: steam ratio in the chemical looping production of hydrogen using Ca2Fe2O5. *Chemical Engineering Journal* **2016,** *296*, 406-411.
36. Antao, S. M.; Hassan, I.; Parise, J. B., Cation ordering in magnesioferrite, MgFe2O4, to 982 C using in situ synchrotron X-ray powder diffraction. *American Mineralogist* **2005,** *90* (1), 219-228.
37. Suchomski, C.; Breitung, B.; Witte, R.; Knapp, M.; Bauer, S.; Baumbach, T.; Reitz, C.; Brezesinski, T., Microwave synthesis of high-quality and uniform 4 nm ZnFe2O4 nanocrystals for application in energy storage and nanomagnetics. *Beilstein J Nanotechnol* **2016,** *7*, 1350-1360.
38. Thanh, N. K.; Loan, T. T.; Duong, N. P.; Anh, L. N.; Nguyet, D. T. T.; Nam, N. H.; Soontaranon, S.; Klysubun, W.; Hien, T. D., Cation distribution assisted tuning of magnetization in nanosized magnesium ferrite. *physica status solidi (a)* **2018,** *215* (1), 1700397 - 1700404.
39. Kidambi, P. R.; Cleeton, J. P.; Scott, S. A.; Dennis, J. S.; Bohn, C. D., Interaction of iron oxide with alumina in a composite oxygen carrier during the production of hydrogen by chemical looping. *Energy & fuels* **2012,** *26* (1), 603-617.
40. Lau, C. Y.; Dunstan, M. T.; Hu, W.; Grey, C. P.; Scott, S. A., Large scale in silico screening of materials for carbon capture through chemical looping. *Energy & Environmental Science* **2017,** *10* (3), 818-831.
41. Huang, L.; Zheng, Q.; Louis, B.; Wang, Q., A facile Solvent/Nonsolvent Preparation of Sintering‐Resistant MgO/CaO Composites for High‐Temperature CO2 Capture. *Energy Technology* **2018,** *6* (12), 2469-2478.
42. Liu, W., Dennis, J.S., Scott, S.A., The Effect of Eddition of ZrO_2 to Fe_2O_3 for Hydrogen production by Chemical Looping. *Industrial & Engineering Chemistry Research* **2012,** *51* (51), 16597-16609.

TOC GRAPHIC

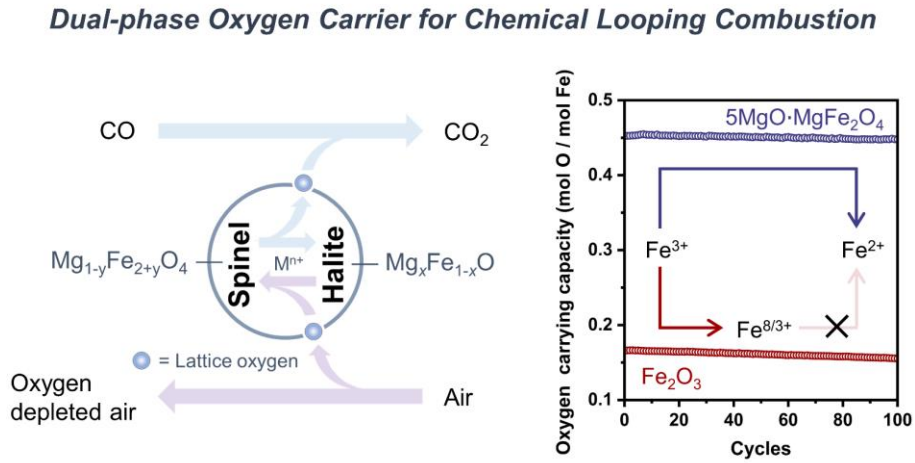

SYNOPSIS

Mg-doping promotes the reactivity and the cyclic stability of Fe-based oxygen carrier with optimized composition for chemical looping combustion.